Manara
Qatar Research
Repository
by Qatar National Library

Novel polysulfone ultrafiltration membranes incorporating polydopamine functionalized graphene oxide with enhanced flux and fouling resistance

Abedalkader Alkhouzaam, Hazim Qiblawey

Item type
Journal Contribution

Terms of use
This work is licensed under a CC BY 4.0 license

This version is available at
https://manara.qnl.qa/articles/journal_contribution/Novel_polysulfone_ultrafiltration_membranes_incorporating_polydopamine_fun
Access the item on Manara for more information about usage details and recommended citation.

Posted on Manara – Qatar Research Repository on
2021-02-15

Journal of Membrane Science 620 (2021) 118900

Contents lists available at ScienceDirect

Journal of Membrane Science

journal homepage: http://www.elsevier.com/locate/memsci

Novel polysulfone ultrafiltration membranes incorporating polydopamine functionalized graphene oxide with enhanced flux and fouling resistance

Abedalkader Alkhouzaam, Hazim Qiblawey *

Department of Chemical Engineering, College of Engineering, Qatar University, P. O. Box 2713, Doha, Qatar

ARTICLE INFO

Keywords:
Ultrafiltration
Dopamine
Graphene oxide
Fouling
Characterization

ABSTRACT

Novel PSF composite UF membranes incorporating low loadings of polydopamine-functionalized graphene oxide particles (rGO-PDA) were fabricated and investigated. The functionalization was confirmed using FTIR-UATR, Raman spectra, XPS, and SEM. Pristine PSF, PSF/GO, and PSF/rGO-PDA MMMs were then prepared using the phase inversion technique and analysed using FTIR, SEM, AFM, and contact angle (CA). The cross-section SEM images showed better distribution of rGO-PDA particles in the pores and polymer wall whereas the pristine GO particles aggregate and partially block the pores. Thus, the pure water flux increased with the addition of rGO-PDA without affecting the rejection properties, while the flux decreased with the embedding of pristine GO particles. The highest pure water permeability (PWP) was obtained with PSF/rGO-PDA-0.1 to be approximately twice that of the pristine PSF and PSF/GO-0.1. All membranes exhibited complete rejection of BSA and HA, and showed almost similar performance against different dyes. The FRRs of the pristine PSF after three fouling cycles (FRR_3) against BSA and HA were recorded to be 57.8% and 70.7% respectively. FRR_3 was enhanced by around 30% with PSF/rGO-PDA composites. The MMMs prepared in this work are expected to have great potential on ultrafiltration and similar studies on other membrane processes.

1. Introduction

The limitation of water resources with the huge increase in population generates a critical problem to water security globally [1] and suitable solutions must be developed to align consumption and supply over time while protecting water quality. Several technologies have been developed over the years to provide alternative water supplies by wastewater treatment, recycle and seawater desalination. Amongst the various methods developed for water treatment, membrane-based technologies have gained wide acceptance due to their low cost, high efficiency, and ease of operation [2].

Membrane-based water treatment is considered a promising solution to provide affordable clean water [3]. Among the different membrane technologies, ultrafiltration (UF) membranes showed significant input in the clean water production. Because of the relatively low-cost, UF is considered economical and efficient pretreatment process for nanofiltration (NF) and reverse osmosis (RO) and can separate wide range of pollutants from wastewater [4]. It is a clean, safe, easily operated, and high-efficient in separating organic substances, proteins, bacteria, viruses, and turbidity. Developing new membrane materials with high separation efficiency and fouling resistance was the focus of most studies in water treatment. Fouling is considered as the most critical challenge in this field that restrict membranes industrial applications [5]. The use of nanotechnology is one of the well investigated methods to produce antifouling membranes with high separation performance [6]. Several nanoparticles were used as nanofillers in the UF mixed matrix membranes (MMMs) such as graphene based materials, metal organic frame works (MOFs), zeolites, carbon nanotubes (CNTs), nano-silica (SiO_2), etc. and they show excellent performance in terms of flux, rejection or fouling resistance [7]. Amongst the various nanoparticles, graphene oxide (GO) and GO-based materials were considered as promising nanofillers that can enhance the membrane's fouling resistance and separation performance owing to the high chemical stability, mechanical strength, and ease of accessibility [6]. The embedding of pristine GO particles was reported to improve the fouling resistance in few studies [8,9]. However, many studies reported a limited fouling resistance against protein fouling of membranes incorporating pristine GO resulting in low flux recovery ratio (FRR<80%) [10–12]. Furthermore, some studies reported a low flux of pristine GO-based membranes which can be related to the aggregation of GO particles due to their poor dispersion in some solvents [13]. Therefore, a successful functionalization and/or

* Corresponding author.
E-mail address: hazim@qu.edu.qa (H. Qiblawey).

https://doi.org/10.1016/j.memsci.2020.118900
Received 6 October 2020; Accepted 3 November 2020
Available online 11 November 2020
0376-7388/© 2020 The Authors. Published by Elsevier B.V. This is an open access article under the CC BY license (http://creativecommons.org/licenses/by/4.0/).

Nomenclature

J_w	Pure water flux (L m^{-2} h^{-1}, LMH)
PWP	Pure water permeability (L m^{-2} h^{-1} bar^{-1}, LMH/bar)
FRR_x	Flux recovery ratio for cycle x
J_{w0}	Initial pure water flux (LMH)
J_{wf}	Foulant water flux (LMH)
J_{w1}	Pure water flux after cleaning
R_t	Total fouling ratio
R_r	Reversible fouling ratio
R_{ir}	irreversible fouling ratio
V	Permeate volume (L)
A	Effective membrane area (m^2)
t	Filtration time (h)
Q	Volumetric flowrate (L h^{-1})
C_p	Solute concentration in the permeate
C_f	Solute concentration in the feed
R	Solute rejection (%)
ΔP	Trans-membrane pressure difference (bar)
Ɛ	Membrane porosity (%)
w_w	The weight of the wet membrane sample (g)
w_d	The weight of the dry membrane sample (g)
l	Membrane thickness (cm)
ρ_w	Water density (0.998 g cm^{-3})
r_m	Mean pore size (nm)
η	Water viscosity (9.3×10^{-4} Pa s)
C/O	Carbon/oxygen atomic ratio
CA	Contact angle (°)
SEM	Scanning electron microscope
AFM	Atomic force microscopy
XPS	X-ray photoelectron spectrometer
FTIR-UATR	Fourier transform infrared spectroscopy-universal attenuated total reflectance sensor
UF	Ultrafiltration
NF	Nanofiltration
RO	Reverse osmosis
MMMs	Mixed matrix membranes
NOM	Natural organic matter
GO	Graphene oxide
rGO	Reduced graphene oxide
GOQD	Graphene oxide quantum dots
MOfs	Metal organic frame works
CNTs	Carbon nanotubes
PES	Polyethersulfone
PSF	Polysulfone
PVDF	Polyvinylidene difluoride
DA	Dopamine
PDA	polydopamine
rGO-PDA	Polydopamine functionalized reduced graphene oxide
PVP	Polyvinylpyrrolidone
NMP	1-methyl-2-pyrrolidone
BSA	Bovine serum albumin
HA	Humic acid
MB	Methyl Blue
SO	Safranine O
ORII	Orange II Sodium salt
DR80	Direct Red 80
Tris	tris-(hydroxymethyl)aminomethane
CSGO	cysteine functionalized graphene oxide
GFG	Guanidyl-functionalized graphene oxide
PES	Polyethersulfone
PVC	Polyvinyl chloride
PEI	Polyethylenimine
CGO	Crumpled graphene oxide
APTS	3-aminopropyltriethoxysilane
BPPO	brominated poly(2,6-dimethyl-1,4-phenylene oxide)
SPSF	Sulfonated polysulfone

the combination of GO particles with other functional materials could enhance their dispersion properties allowing them to achieve their highest potential for improving the performance and antifouling properties of GO-based membranes [14]. Some GO-based materials exhibited enhancement in flux, rejection and fouling resistance. For example, Zhang et al. [15] reported that the flux of polysulfone (PSF) composite membranes incorporating guanidyl-functionalized GO particles (GFG) exhibited 1.6 times higher flux than PSF composites incorporating pristine GO particles accompanied with high BSA rejection (95.2%) and FRR (82.4%). The authors linked this enhancement to the higher hydrophilicity of GFG particles compared to pristine GO particles that improved the pore structure of PSF. Similar findings were obtained with polyvinylidene fluoride (PVDF) incorporating GO-TiO_2 nanocomposite particles with FRR of 89.22% against BSA accompanied with pure water permeability (PWP) of 199.97 LMH/bar and 91.38% BSA rejection. On the other hand, some functional GO-based MMMs exhibit a tradeoff between flux, rejection and FRR. Xu et al. [16] functionalized GO particles with 3-aminopropyltriethoxysilane (APTS) and then embedded them into PVDF using the phase inversion approach. The FRR of PVDF/GO-APTS composite membranes against BSA was about 1.7 and 1.1 times higher than the FRR of pristine PVDF and PVDF/GO, respectively. This was attributed to the high hydrophilicity and dispersibility of GO-APTS in the PVDF pore channels, which made the pollutants washed away by water easily. However, the BSA rejection was 57%, which is considered low for such large molecules. In contrast to this, some GO-based MMMs exhibited high rejection and FRR accompanied with low flux like PES/CSGO [17] and PSF/CGO [13]; or high flux and rejection with low FRR such as PSF/Isocyanate-GO [18]. Therefore, exploring new ways of GO functionalization to produce GO particles of high hydrophilicity and dispersibility will pave the way for the development of new MMMs with high flux, rejection and antifouling properties.

In 2007, dopamine (DA), a unique mussel-inspired biomolecule, was found to undergo self-polymerization in mild alkaline media producing thin film (polydopamine) that can be easily adhered on different materials [19]. Because of the abundant functional groups like amine, catechol, and imine [20] on its surface, polydopamine (PDA) is considered a versatile platform for additional modification with the various functional groups [21]. Therefore, PDA has been extensively utilized for different coating applications like membranes [22,23], anticorrosion coatings [24] sensors and semiconductors [25,26]. Owing to the high adhesion properties of PDA, it can be easily attached and grafted on the surface and between GO sheets to form reduced graphene oxide particles (rGO) with extreme hydrophilicity and dispersity in various organic solvents [27,28]. The simultaneous utilization of GO and PDA in the synthesis and functionalization of UF membranes was reported in several studies [29–31]. However, all of these membranes were prepared by the physical assembly approaches leading to poor mechanical stability of the membrane because of the weak interface between the adjacent layers [6]. Although the stability of the assembled GO membranes can be improved using various cross-linkers [1], these crosslinkers usually lead to a reduction in the membrane flux. In contrast, the embedding of GO-based particles into the polymer matrix was found to have better stability in harsh environments accompanied with flux, rejection, and antifouling enhancement [1].

Therefore, in this work we report a novel ultrafiltration polysulfone

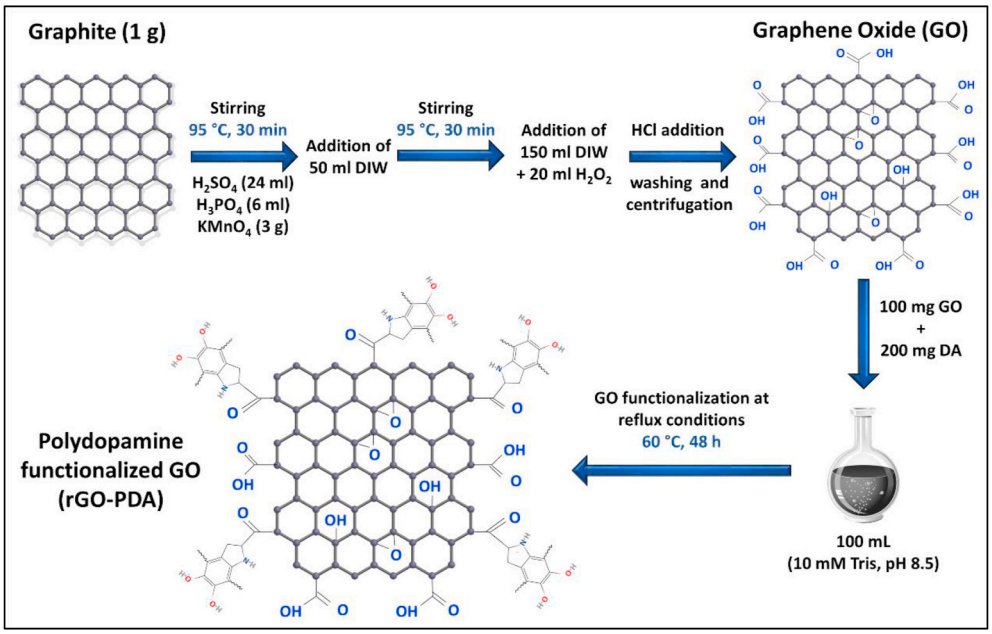

Fig. 1. Illustration of the GO synthesis and functionalization procedures.

(PSF) mixed matrix membranes (MMMs) incorporating PDA functionalized rGO particles (rGO-PDA) with high flux, rejection and fouling resistance against organic and protein fouling. GO particles were firstly reduced and functionalized during the dopamine self-polymerization using a simple temperature-assisted reflux method. Two sets of MMMs were then fabricated incorporating the pristine GO (PSF/GO) and the functionalized GO particles (PSF/rGO-PDA) with different concentrations via the phase inversion approach. The prepared nanoparticles and membranes were characterized using different analytical techniques to investigate the effect of PDA functionalization on GO properties and on the membranes structural and morphological properties. The performance of the prepared membranes in terms of flux, rejection, protein and organic fouling resistance were investigated in a cross-flow membrane apparatus. Taken together, results afford insights on how the differences between the pristine GO and the functionalized GO affect the membrane structure, performance, and antifouling properties. To the authors knowledge, the use of rGO-PDA nanoparticles in the fabrication of UF MMMs and the investigation of their effects on the membranes performance and fouling resistance has not been investigated in literature yet.

2. Experimental details

2.1. Materials

Graphite flakes were obtained from Alfa Aesar, Germany (−10 mesh, 99.9%). Sulfuric acid (H_2SO_4, 95%), Polyvinylpyrrolidone (PVP, ≥ 95%), and potassium permanganate ($KMnO_4$,99%) were obtained from Fisher Scientific. Hydrochloric acid (HCl, 35–38%), phosphoric acid (H_3PO_4, 99%), Safranine O (SO, 350.88 Da), Methyl Blue (MB, 799.81 Da) and hydrogen peroxide (H_2O_2, 30%) were obtained from BDH. Polysulfone (PSF, ~35 kDa), dopamine hydrochloride (DA), tris-(hydroxymethyl)aminomethane (Tris), humic acid (HA), bovine serum albumin (BSA, ≥ 96%, Mw ~ 66 kDa), Direct Red 80 (DR80, 1373.07 Da), Orange II sodium salt (ORII, 350.32 Da), and 1-Methyl-2-pyrrolidinone (NMP, 99.5%) were obtained from Sigma Aldrich. A Milli-Q ultrapure purification system was used to produce deionized water (DIW). All chemicals were used as procured without further purification.

2.2. Graphene oxide synthesis and functionalization

Graphene oxide has been synthesized using an improved Hummers' method described elsewhere [32]. In brief, the oxidation of graphite was conducted using a mixture of 24 mL H_2SO_4 and 6 mL of H_3PO_4. Graphite flakes (1 g) and $KMnO_4$ (3 g) were then slowly added to the acid mixture when placed in an ice bath. The mixture was then transferred to an oil bath and kept stirring at 95 ± 2 °C for 30 min 50 mL of DIW was then added and the mixture and kept stirring under the same conditions for another 30 min. The mixture was then transferred to an ice bath where 150 mL of DI and 20 mL of H_2O_2 were added slowly to terminate the oxidation process. The resulted solution was then diluted and washed with 20% HCl solution and then centrifuged for 20 min at 7500 rpm (Ohaus Frontier 5000 Series Multi Pro Centrifuge). Then, the solution was washed and centrifuged several times with DIW until the pH became neutral. Finally, the resulted sample was dried in oven at 80 °C for about 48 h.

The functionalization of GO with PDA was conducted using the temperature-assisted reflux technique. In brief, 200 mg PDA and 100 mg GO were dispersed in a 10 mM Tris solution (100 mL, pH 8.5) using an ultra-sonication bath for 1 h. The suspension was then transferred to an oil bath and kept stirring at 60 °C for 48 h under reflux conditions. The PDA functionalized GO particles (rGO-PDA) were then extracted via the solvent evaporation technique and were then dried overnight in a vacuum oven at 80 °C. Fig. 1 illustrates the synthesis procedures of GO, the functionalization reaction with PDA, and the expected chemical structure of rGO-PDA.

2.3. Membranes fabrication

The preparation of the pristine PSF, PSF/GO and PSF/rGO-PDA composite membranes was conducted using the phase inversion technique [13]. Briefly, a 17 wt% PSF in NMP was used as the casting solutions with 3 wt% PVP (3 wt%) as pores forming agent. First, two stock dispersions of GO and rGO-PDA in NMP were prepared with concentration of 0.5 mg/mL using an ultra-sonication bath for approximately 1 h to ensure well dispersion. Different concentrations of GO and rGO-PDA were then prepared (with respect to PSF) from the stock dispersions by dilution. GO-NMP and rGO-PDA-NMP suspensions were then stirred under room temperature. PVP and PSF were then loaded slowly to the

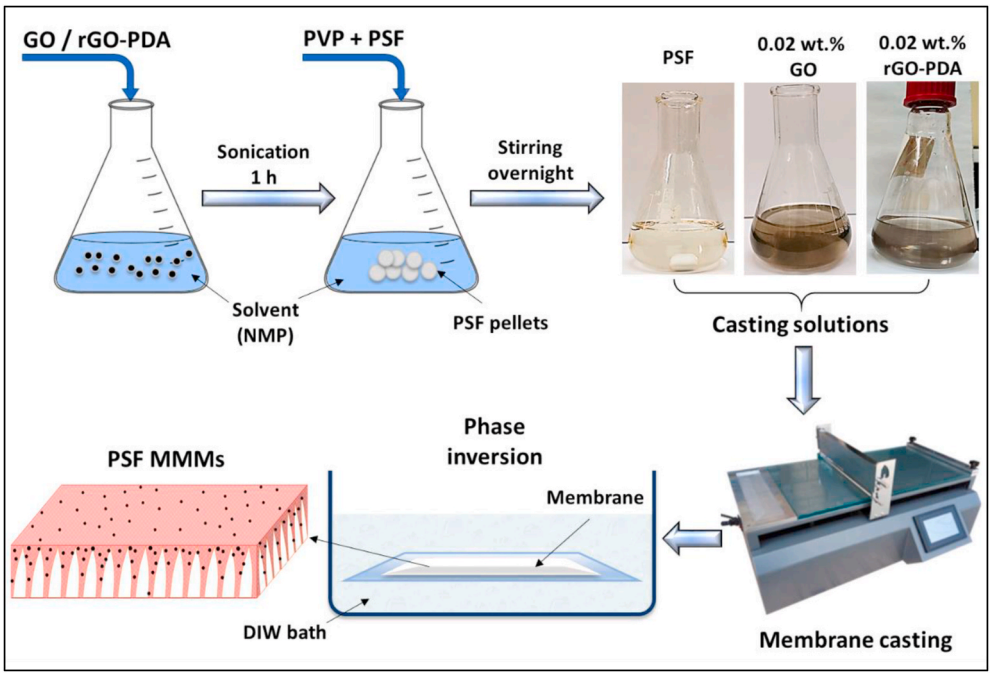

Fig. 2. Illustration of the fabrication process of pristine PSF, PSF/GO and PSF/rGO-PDA MMMs via phase inversion technique.

Table 1
GO and rGO-PDA compositions in the prepared membranes.

Code	Membrane	PSF (g)	PVP (g)	NMP (mL)	Stock dispersion (mL)	GO (wt %)[a]	rGO-PDA (wt %)[a]
M_0	PSF	5.53	0.975	25	0	–	–
M_{GO1}	PSF/GO-0.02	5.53	0.975	23	2 (GO)	0.02	–
M_{GO2}	PSF/GO-0.05	5.53	0.975	20	5 (GO)	0.05	–
M_{GO3}	PSF/GO-0.1	5.53	0.975	14	11 (GO)	0.1	–
M_{GO4}	PSF/GO-0.15	5.53	0.975	8	17 (GO)	0.15	–
M_{PDA1}	PSF/rGO-PDA-0.02	5.53	0.975	23	2 (rGO-PDA)	–	0.02
M_{PDA2}	PSF/rGO-PDA-0.05	5.53	0.975	20	5 (rGO-PDA)	–	0.05
M_{PDA3}	PSF/rGO-PDA-0.1	5.53	0.975	14	11 (rGO-PDA)	–	0.1
M_{PDA4}	PSF/rGO-PDA-0.15	5.53	0.975	8	17 (rGO-PDA)	–	0.15

[a] The compositions of GO and rGO-PDA are with respect to PSF weight.

solution and kept under stirring conditions overnight to allow complete dissolving of the polymer and uniform dispersion of the nanoparticles. The resulted well mixed solutions were then casted on a clean glass plate using an Elcometer 3700 doctor blade (Elcometer Ltd, UK). The casted membranes were then dipped into DIW bath after casting to allow ideal phase inversion. Theses membranes were then washed several times and stored in DIW until usage. Fig. 2 illustrates the fabrication process of the pristine PSF and PSF MMMs incorporating GO and rGO-PDA via the phase inversion technique. The notations and compositions of the prepared membranes are listed in Table 1.

2.4. Characterization of GO and rGO-PDA particles

The prepared GO and rGO-PDA were characterized using several techniques to confirm the oxidation of graphite and the success of functionalization/reduction reaction. FTIR-UATR spectra were determined using FTIR PerkinElmer 2000 to study the functional groups presented in each sample. Raman spectra were determined using a DXR Raman Spectrometer (Thermo Scientific) equipped with a 532 nm laser and a 10 × objective. X-ray photoelectron spectroscopy (XPS) was conducted using AXIS Ultra DLD, Kratos equipped with Al-Kα source with X-ray power of 15 Kv and 20 mA. Moreover, GO and rGO-PDA morphology was evaluated using scanning electron microscopy (SEM) using JEOL model JSM-6390LV.

2.5. Characterization of the membranes

Different characterization techniques were performed on the prepared MMMs to explore the effect of GO/rGO-PDA incorporation on the structural and morphological properties of PSF. FTIR-UATR spectra were determined to investigate the change in surface chemical structure. Cross-section and surface SEM images were obtained at different magnifications. To prepare the cross-section samples, the freeze-fracturing method was used to avoid the deformation of the membrane structure by freezing the prepared membranes in liquid nitrogen and breaking them immediately [33]. Atomic force microscopy (AFM) measurements were conducted using (AFM-MFP-3D, Asylum Research) over 10 × 10 μm scan area with a scan rate of 1 Hz. The hydrophilicity of the prepared membranes was investigated using DataPhysics contact angle analyzer (OCA15 Pro, Germany). Minimum of 15 points of each sample were tested using DIW droplet of 2 μm at room temperature and the average CA value were recorded. The viscosity of the dope solutions was measured at room temperature (Anton Paar Rheometer Model MCR 302) to investigate the effect of GO and rGO-PDA embedding on the casting solution viscosity.

2.6. Porosity and mean pore size determination

The overall porosity (Ɛ) of the prepared membranes was determined using the gravimetric method as described by Eq. (1) [13]:

$$\varepsilon = \frac{w_w - w_d}{A \times l \times \rho_w} \quad (1)$$

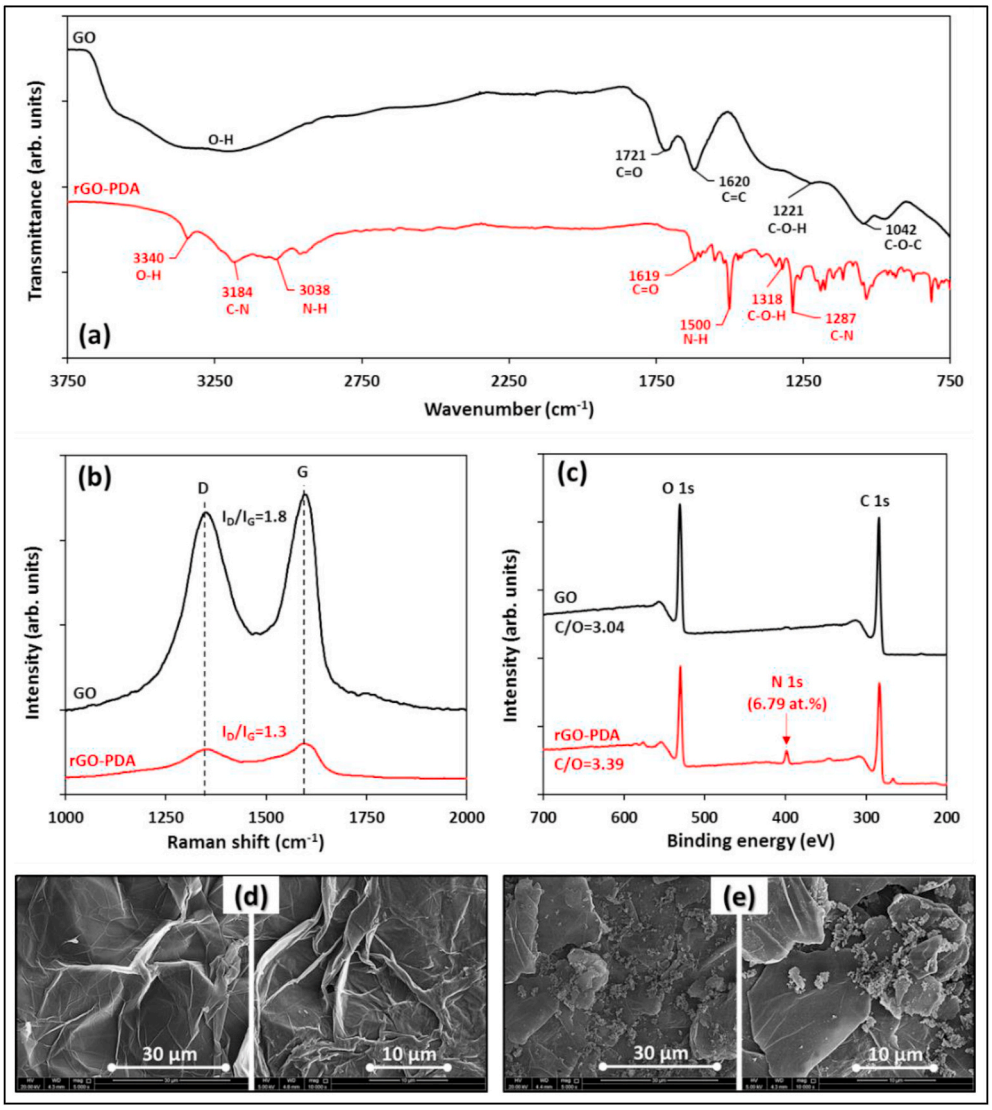

Fig. 3. (a) FTIR-UATR spectra, (b) Raman spectra, (c) XPS survey spectra of GO and rGO-PDA; (d) and (e) SEM images of GO and rGO-PDA, respectively.

where w_w is the weight of the wet membrane (g), w_d is the weight of the dry membrane (g), A is the surface area of the membrane (cm^2), l is the membrane thickness (cm) determined from the cross-section SEM (Fig. S1 of the supplementary information), and ρ_w is the water density at 23 °C (0.998 g cm^{-3}). The mean pore size (r_m) was then determined using the Guerout-Elford-Ferry equation (Eq. (2)) [16,34]:

$$r_m = \sqrt{\frac{(2.9 - 1.75\varepsilon) \times 8\eta l Q}{\varepsilon \times A \times \Delta P}} \quad (2)$$

where η is the water viscosity at 23 °C (9.3×10^{-4} Pa s), Q is the permeate flow rate ($m^3.s^{-1}$), and ΔP is the operational pressure (Pa).

2.7. Permeability and separation experiments

The separation performance and antifouling properties of the prepared membranes were studied using a commercial cross-flow membrane apparatus (Sterlitech Corp, US) equipped with a temperature control system. Flux (J_w, LMH), pure water permeability (PWP, LMH/bar) and rejection (R%) were calculated using Eqs. (3)–(5), respectively [21].

$$J = \frac{V}{A.t} \quad (3)$$

$$PWP = \frac{Q}{\Delta P.A} \quad (4)$$

$$R(\%) = 1 - \left(\frac{C_p}{C_f}\right) \times 100 \quad (5)$$

where V is the permeate volume (L), A is the effective membrane area if the membrane (m^2), t is the operating time (h), Q is the volumetric flowrate of the permeate ($L.h^{-1}$), ΔP is the trans-membrane pressure difference, C_p and C_f are the solute concentration in the permeate and feed respectively.

The rejection properties of the prepared membranes were evaluated using different dyes including Safranine O (SO), Orange II sodium salt (ORII), Methyl Blue (MB) and Direct Red 80 (DR80). The dyes rejection tests were performed at 1 bar with 25 ppm dye concentration in the feed. The concentrations of feed and permeate, C_f and C_p, were measured using UV-VIS spectrophotometer (UV-2700, Shimadzu) at wavelengths of 520, 485, 600, and 528 nm for SO, ORII, MB, and DR80, respectively.

2.8. Dynamic fouling experiments

Antifouling properties of the prepared UF membranes were investigated using 500 mg/L BSA and 25 mg/L HA as the model foulants

representing protein and natural organic matters (NOMs) fouling (each foulant was studied separately). Three dynamic fouling cycles were conducted for each membrane. In brief, the membrane was compacted with DIW at 4 bar for 30 min. The pressure was then reduced to 1 ± 0.1 bar with cross-flow velocity of 46.1 ± 0.3 cm s^{-1} and the steady pure water flux was recorded (J_{w0}). The feed is then shifted to freshly prepared foulant solution at the same pressure and cross-flow velocity for 1 h and the foulant flux (J_{wf}) was then recorded. After foulant filtration, the membrane was washed two times with DIW at the same cross-flow velocity without applied pressure for 30 min. Finally, the feed is shifted to pure DIW at 1 bar and the steady flux was recorded (J_{w1}). The total fouling ratio (R_t), flux recovery ratio (FRR), the reversible fouling ratio (R_r) and the irreversible fouling ratio (R_{ir}) were estimated using equations (6)–(9), respectively [22]:

$$R_t(\%) = \frac{J_{w0} - J_{wf}}{J_{w0}} \times 100 \quad (6)$$

$$FRR\ (\%) = \frac{J_{w1}}{J_{w0}} \times 100 \quad (7)$$

$$R_r(\%) = \frac{J_{w1} - J_{wf}}{J_{w0}} \times 100 \quad (8)$$

$$R_{ir}(\%) = \frac{J_{w0} - J_{w1}}{J_{w0}} \times 100 \quad (9)$$

The second and third cycles were conducted by repeating the same steps of cycle 1, and the corresponding FRR_x was recorded for each cycle, where x is the cycle number. The concentrations of BSA and HA in the feed and permeate, C_f and C_p, were measured using UV-VIS spectrophotometer (UV-2700, Shimadzu). BSA concentration was measured at 278 nm [35], while HA concentration was measured at 254 and 280 nm [36]. All separation and antifouling experiments were performed at room temperature (23 ± 0.5 °C). Minimum of three samples of each membrane were tested and the average value was taken for all performance and fouling parameters.

3. Results and discussion

3.1. Characterization of GO and rGO-PDA particles

The FTIR-UATR spectra of the GO and rGO-PDA particles are presented in Fig. 3a. The oxidation of graphite is confirmed from the presence of several bands in the GO spectra corresponding to oxygen functionalization including epoxy C–O–C stretching vibration, C–OH bending vibrations of the hydroxyl groups, and C = = O stretching vibration of the carbonyl functional groups on the edge of GO sheets at ~1042, 1221, and 1721 cm^{-1}. The C═C skeletal vibration around 1620 cm^{-1} corresponds to the unoxidized graphene [37] while the O–H stretching vibration around 3250 cm^{-1} corresponds to the water molecules trapped between GO sheets [32].

The spectra of rGO-PDA confirm the successful functionalization of GO with the PDA by the presence of several bands at 3184, 3038, 1619, 1500, and 1287 cm^{-1}. These bands were reported in some studies and were related to the amide functionality of PDA [38]. It can be clearly seen that the C = = O band of GO (~ 1707 cm^{-1}) was disappeared after the functionalization with PDA indicating a clear reduction of GO to rGO [39] which is consistent with the expected rGO-PDA chemical structure in Fig. 1.

Raman spectra presented in Fig. 3b show that the two characteristic bands of GO particles, D and G, are presented in both spectra around 1350 and 1590 cm^{-1}, respectively. The ratio of the relative intensities of D and G bands (I_D/I_G) was estimated to be 1.8 and 1.3 for GO and rGO-PDA, respectively, suggesting a clear change in the crystallite size and structure of the GO particles due to the functionalization reaction [32,40]. The XPS survey spectra of GO and rGO/PDA are shown in Fig. 3c.

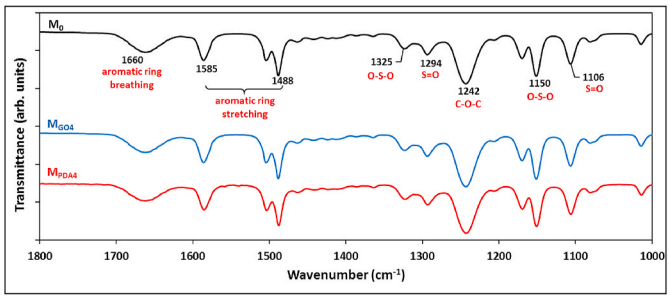

Fig. 4. FTIR-UATR spectra of M_0, M_{GO4}, and M_{PDA4} membranes.

Both spectra show the presence of C 1s and O 1s core-levels at binding energies of ~ 284 and 531 eV, respectively. The rGO-PDA spectra show an emerging peak at a binding energy of 398 eV corresponding to the N 1s core-level (6.79 at%) which indicates a successful amination of GO particles. Further, the carbon/oxygen (C/O) atomic ratio increased from 3.04 to 3.39 with the amination of GO particles indicating a partial reduction of GO which is in a good agreement with the FTIR findings. Fig. 3d and e presents the SEM images of GO and rGO-PDA, respectively, at different magnifications. The SEM images show clear differences in the morphological structure of GO and rGO-PDA. Images of the pristine GO show sharp, clear and smoother flakes whereas the surface became rough with irregular structure after the functionalization with PDA. The distribution and attachment of PDA particles on the GO sheets can be clearly seen in the SEM images at 10,000× magnifications confirming the morphological change due to the functionalization reaction.

3.2. Characterization of membranes

FTIR-UATR spectra of the control PSF (M_0), M_{GO4}, and M_{PDA4} as an example are shown in Fig. 4. The spectra of other membranes are presented in Fig. S2 of the supplementary information. Spectra for all membranes show the characteristic bands of polysulfone that have been reported in literature [41,42]. The following functional groups were identified in the spectra of the prepared membranes: S═O stretching (~ 1106 cm^{-1}), O–S–O symmetric stretching (~1150 cm^{-1}), C–O–C stretching (~1242 cm^{-1}), S═O stretching (~ 1294 cm^{-1}), O–S–O asymmetric stretching (~ 1320 cm^{-1}), aromatic ring stretching (~ 1488, 1588 cm^{-1}), and aromatic ring breathing (~ 1660 cm^{-1}). No obvious difference was found in the spectra of PSF and PSF composites due to the low concentration of GO and rGO-PDA and the dominance of PSF in the membrane matrix. Similar observations were reported with PSF MMMs incorporating low loadings of GO particles [13].

The surface and cross-section SEM images of the prepared membranes were obtained at different magnifications to study the effect of GO and rGO-PDA embedding on the PSF structure. The surface and cross-section SEM images of the pristine PSF, PSF/rGO-PDA-0.02, and PSF/GO-0.02 are presented in Fig. 5. The SEM images of the other PSF/GO and PSF/rGO-PDA composite membranes are presented in Figs. S3 and S4 in the supplementary information, respectively. The surface SEM images do not show significant difference between the pristine PSF and PSF composites. However, the cross-section SEM images exhibited clear influence of GO and rGO-PDA embedding onto the PSF structure. Two distinct layers can be observed in all membranes: a thin dense layer on the top and a typical sponge structure sub-layer. The sub-layer consists of several finger-like macro-voids and small pores surrounded by the polymer wall. With the addition of GO and rGO-PDA particles, the finger-like macro-voids became wider and longer because of the hydrophilicity of GO and rGO-PDA that increase the mass transfer rate between the solvent (NMP) and non-solvent (water) during phase inversion process [43]. Similar observations were reported in several studies in literature [18,44]. At high magnifications, it can be clearly seen that both GO and rGO-PDA particles are distributed on the polymer

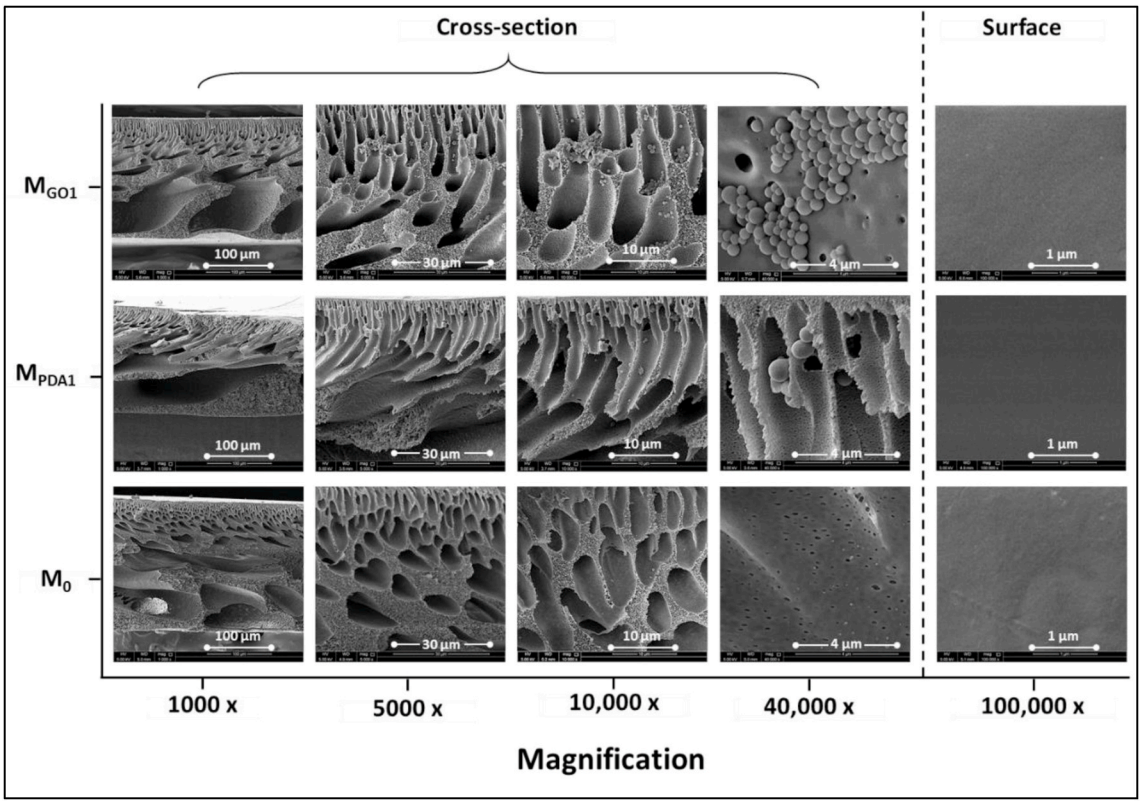

Fig. 5. Surface and cross-section SEM images of M_0, M_{PDA1}, and M_{GO1} membranes.

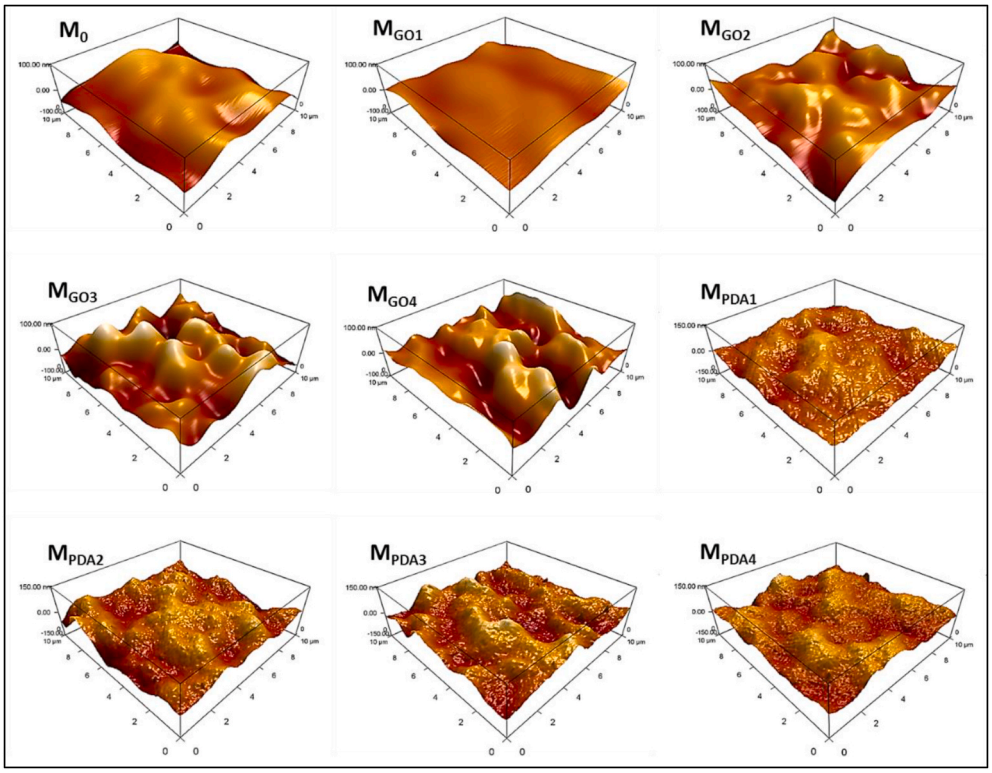

Fig. 6. AFM images of the pristine PSF, PSF/GO and PSF/rGO-PDA composite membranes.

wall of the sub-layer with spherical shape. Similar observations were previously reported with PEI/GO MMMs [45]. The high magnification SEM images shows also that pristine GO particles are agglomerated in some areas of the sub-layer causing a partial clogging of the membrane pores even at low concentrations (e.g. 0.02 wt% GO). This clogging usually reduces the water flux through the membrane as discussed in the

Table 2
The average values of the membrane thickness (l), porosity (Ɛ), mean pore size (r_m), root-mean-square roughness (RMS), and average roughness (Ra) of the prepared membranes.

Membrane	l (μm)	Ɛ (%)	r_m (nm)	RMS (nm)	Ra (nm)
M_0	205.3 ± 0.5	81.2 ± 0.1	37.5 ± 0.1	9.4 ± 2.3	7.8 ± 2.1
M_{GO1}	188.3 ± 4.2	86.6 ± 5.1	33.7 ± 2.1	6.2 ± 0.8	5.1 ± 0.6
M_{GO2}	174.3 ± 2.6	85.5 ± 0.2	34.4 ± 0.1	14.1 ± 0.9	11.3 ± 0.8
M_{GO3}	255 ± 2.9	82.9 ± 0.1	36.9 ± 0.0	16.2 ± 3.0	13.0 ± 2.5
M_{GO4}	208.9 ± 3.4	79.9 ± 2.8	33.0 ± 1.1	21.6 ± 5.6	16.9 ± 5.4
M_{PDA1}	161.2 ± 3.5	87.7 ± 2.9	37.5 ± 1.6	25.7 ± 3.4	20.6 ± 2.8
M_{PDA2}	206.3 ± 5.1	79 ± 2.1	48.2 ± 2.2	31.0 ± 0.8	24.7 ± 1.2
M_{PDA3}	200.7 ± 0.9	80.5 ± 1.1	50.6 ± 0.9	34.0 ± 0.2	28.2 ± 0.7
M_{PDA4}	210.4 ± 0.5	78.7 ± 0.2	42.7 ± 1.3	27.7 ± 1.3	22.7 ± 1.1

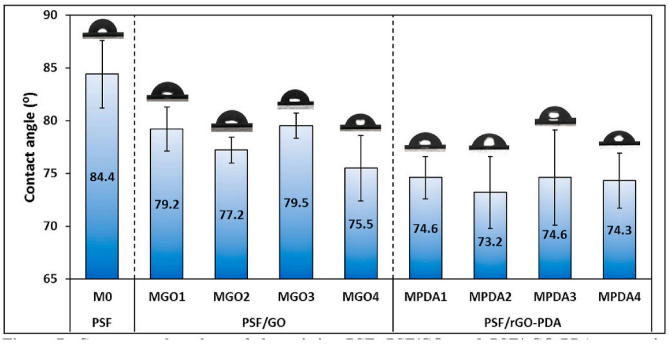

Fig. 7. Contact angle values of the pristine PSF, PSF/GO, and PSF/rGO-PDA composite membranes.

coming sections. On the other hand, the rGO-PDA particles exhibited better distribution without obvious agglomeration which can be related to the higher dispersity of rGO-PDA particles in NMP than the pristine GO. It is worth mentioning that rGO particles were found to have higher dispersity than pristine GO particles in several organic solvents making them ideal nanofillers for different membrane materials [46].

Surface roughness is essential factor that affect the separation and fouling resistance of a membrane. Hence, AFM analysis was conducted to study the effect of GO and rGO-PDA incorporation on membrane roughness. The three-dimensional surface AFM images of PSF, PSF/GO and PSF/rGO-PDA composites over 10 × 10 μm scan area are shown in Fig. 6. The roughness parameters represented by the root-mean-square roughness (RMS) and the average roughness (Ra) are listed in Table 2. Two pieces of each membrane were tested, and the average RMS and Ra values were calculated. The surface roughness was found to increase with the addition of GO and rGO-PDA except for M_{GO1} (PSF/GO-0.02). The RMS and Ra values of pristine PSF were found to be 9.4 and 7.8 nm, respectively, that lie in the range of roughness parameters for other PSF membranes in literature [47,48]. The highest roughness values among the PSF/GO composites were obtained with M_{GO4} (PSF/GO-0.15) with RMS and Ra of 21.6 and 16.9 nm, respectively. On the other hand, the roughness increase was much higher with the addition of rGO-PDA even at low concentrations which can be attributed to the presence of the amine and hydroxyl groups of PDA [49]. The highest roughness among the PSF/rGO-PDA composites was obtained with M_{PDA3} (PSF/rGO-PDA-0.1) with RMS and Ra values of 34.0 and 28.2 nm, respectively. It can be also observed that the roughness decreased with higher loadings of rGO-PDA (M_{PDA4}). This is can be explained by the high viscosity of the casting solution which delays the phase inversion process and result in highly dense surface [42,50]. It is well established that membranes with rough surface have higher surface area which enhance the water flux through the membrane [42]. However, the high roughness could increase the fouling due to the contaminants accumulation in the valleys [51].

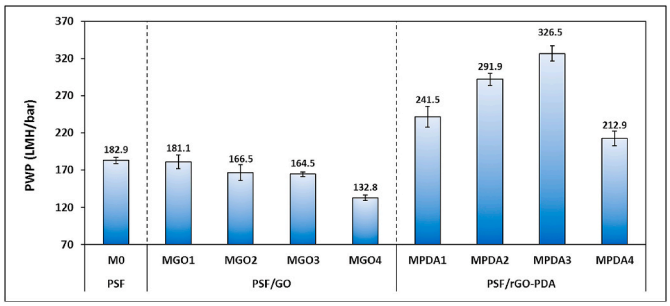

Fig. 8. The PWP (LMH/bar) of the pristine PSF, PSF/GO, and PSF/rGO-PDA composite membranes.

Other parameter that affect the flux and fouling resistance are the membrane porosity, pore size and hydrophilicity. The surface hydrophilicity of the pristine and composite membranes in terms of static contact angle (CA) is illustrated in Fig. 7. Obviously, CA decreased slightly with the addition of GO providing more hydrophilicity to membrane surface. The average CA of pristine PSF was found to be 84.4° while it decreased up to 75.5° with the addition of 0.15 wt% GO. This observation was previously reported in different studies with PSF and other polymers and was related to the hydrophilic nature of GO [8,13,52]. The decrease in CA was more obvious with the addition of rGO-PDA particles. This observation can be linked to the abundant hydroxyl groups of PDA grafted on the surface and between GO sheets [22]. The average CA of PSF/rGO-PDA composite membranes ranged between 73.2° and 74.6°. The observed CA values for both PSF/GO and PSF/rGO-PDA composites are lying in the same range (70°–80°) of other PSF/GO-based MMMs reported in literature [13,18,53]. Although the measured CA values of the membranes do not show significant improvement, the GO and rGO-PDA particles are expected to have more effect on pores hydrophilicity than the surface hydrophilicity. This can be confirmed from the SEM images that show higher distribution of nanoparticles within the membrane pores and polymer wall than this on the surface.

The overall porosity (Ɛ) and the mean pore size (R_m) of the prepared membranes are listed in Table 2. With the addition of 0.02 wt% of GO and rGO-PDA, the porosity of PSF increased from 81.2% to 86.6% and 87.7%, respectively. This can be explained by the increase of mass-transfer rate between the solvent (NMP) and non-solvent (DIW) during the phase inversion process caused by the addition of hydrophilic nanofiller, namely GO and rGO-PDA [54]. However, with further increase of the both nanofillers concentration, the porosity decreases. Excessive loadings of the nanofiller increase the viscosity of the casting solution which delays the de-mixing during the phase inversion process and leads to lower porosity and the formation of smaller pores [42]. The estimated mean pore size (r_m) of PSF/GO composite membranes was lower than this of the pristine PSF. The mean pore size of the pristine PSF was found to be around 37.5 nm while it ranged between 33 and 36.9 nm for PSF/GO composites. This can be linked to the agglomeration of GO particles inside the pores resulting in a partial blockage as evidenced by the cross-section SEM images. Similar observations have been reported with GO-based MMMs in earlier studies [43,45,54]. Conversely, the PSF/rGO-PDA composite membranes exhibited bigger pore sizes than the pristine PSF. This could be attributed to the high dispersibility of rGO-PDA particles in the solvent which prevents the aggregation of rGO-PDA particles inside the pores as confirmed by the SEM images.

3.3. Permeability and separation performance

The pure water permeability (PWP) of the prepared membranes are depicted in Fig. 8. The PWP of the pristine PSF was recorded to be 182.9 ± 4.5 LMH/bar. With low concentration of the pristine GO (0.02 wt%), the PWP was not significantly affected (181.1 ± 9.4 LMH/bar).

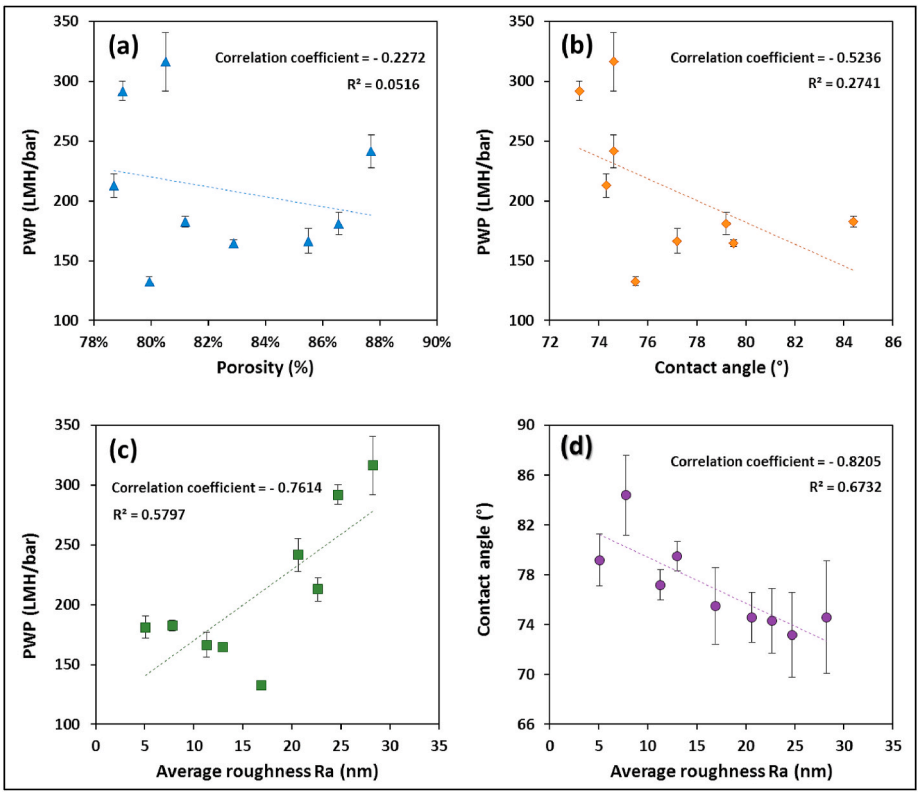

Fig. 9. The correlations of the PWP with (a) porosity (Ɛ), (b) water contact angle (CA), (c) average roughness (Ra), and (d) the correlation of CA with Ra.

However, with further loadings of the GO particles, membranes exhibited clear decreases in PWP to 166.5 ± 10.5, 164.5 ± 2.7, and 132.8 ± 3.7 LMH/bar for M_{GO2}, M_{GO3}, and M_{GO4}, respectively. On the other hand, the PWP was significantly enhanced with the embedding of rGO-PDA particles. The PWP values of PSF/rGO-PDA composite membranes were found to be 241.5 ± 13.7, 291.9 ± 8.1, and 326.5 ± 10.3 LMH/bar for M_{PDA1}, M_{PDA2}, and M_{PDA3}, respectively. The PWP was then decreased to 212.9 ± 10 LMH/bar with excessive loadings of rGO-PDA particles (0.15 wt%). The flux reduction upon high loadings of nanomaterial have been previously reported in several studies [13,52,55] and can be attributed to the presence of a tipping mass percentage of nanofiller [34,56]. The embedding of a hydrophilic nanofiller changes the overall hydrophilicity of the casting solution which accelerates the solvent and non-solvent exchange during phase inversion process. However, excessive loadings of the nanomaterial increase the viscosity of the casting solution resulting in porosity and pore size reduction as shown in the results obtained from porosity and pore size measurements. The tipping mass percentage is a critical point after which the permeability decreases because of the increase in casting solution viscosity [54,56]. It varies depending on the type of nanofiller and polymer [13]. Therefore, the results herein suggest a tipping mass percentage <0.02 wt% for pristine GO and <0.1 wt% for rGO-PDA particles. These findings can be confirmed by the viscosity measurements of the casting solutions of M_0, M_{GO3} and M_{PDA3} presented in Fig. S5 of the supplementary information. The addition of 0.1 wt% GO-PDA increased the viscosity of the casting solution by approximately 11%. However, the viscosity was increased by approximately 76% with the addition of 0.1 wt% pristine GO. Similar observations were recently reported by Alammar et al. [57] where the viscosity increase was higher with pristine GO particles than this with rGO particles. The significant increase in the dope solution viscosity resulted in the formation of a semi-dense top layer leading to the reduction in water flux [12].

Further analysis of the results obtained from PWP, mean pore size, roughness and hydrophilicity measurements helps to elaborate more on the factors affecting the change in PWP. Therefore, a simple data analysis was conducted (Microsoft Excel) to find the correlation coefficient between the PWP and other characteristic parameters including the porosity (Ɛ), average roughness (Ra), and contact angle (CA). The correlation coefficient is a statistical measure that indicates the strength of the linear relationship between two variables by measuring and relating the variance and standard deviation of each variable as shown in Eq. (10).

$$Correl(A,B) = \frac{Covariance(A,B)}{Std.\ Dev\ A \ \times \ Std.Dev\ B} \tag{10}$$

The output of the correlation test is presented in Table S1 of the supplementary information. Fig. 9 depicts the plots of the PWP against other parameters. The findings suggest that the PWP, of membranes studied herein, is more affected by the average roughness with a correlation factor of 0.7614 (Fig. 9c) followed by CA with slight correlation of −0.5236 (Fig. 9b); while a weak correlation with the porosity was observed as shown in Fig. 9a. Fig. 9d shows that CA is affected by the surface roughness with a correlation factor of −0.8205. This simple analysis is suggesting a dominance of the surface roughness (Ra) on the water permeability compared to other factors like contact angle and membrane porosity. This agrees with some findings in the literature [58,59], while other studies showed the porosity to have higher impact on the membrane permeability [13,60].

The separation performance was studied by the filtration of 500 ppm BSA and 25 ppm HA solutions. All tested membranes, including the pristine PSF, exhibited a complete rejection of both BSA and HA (virtually 100%). Similar findings have been reported by different studies [9,36,42,61]. Generally, the rejection mechanisms in membranes include sieving (size-based), charge, and adsorption-based mechanisms. However, for UF membranes, sieving is considered the key mechanism of rejection. Hence, the rejection of both BSA and HA is mainly a size-based filtration mechanism due to their high molecular weights [13]. The rejection performance of M_0, M_{GO3}, and M_{PDA3} with

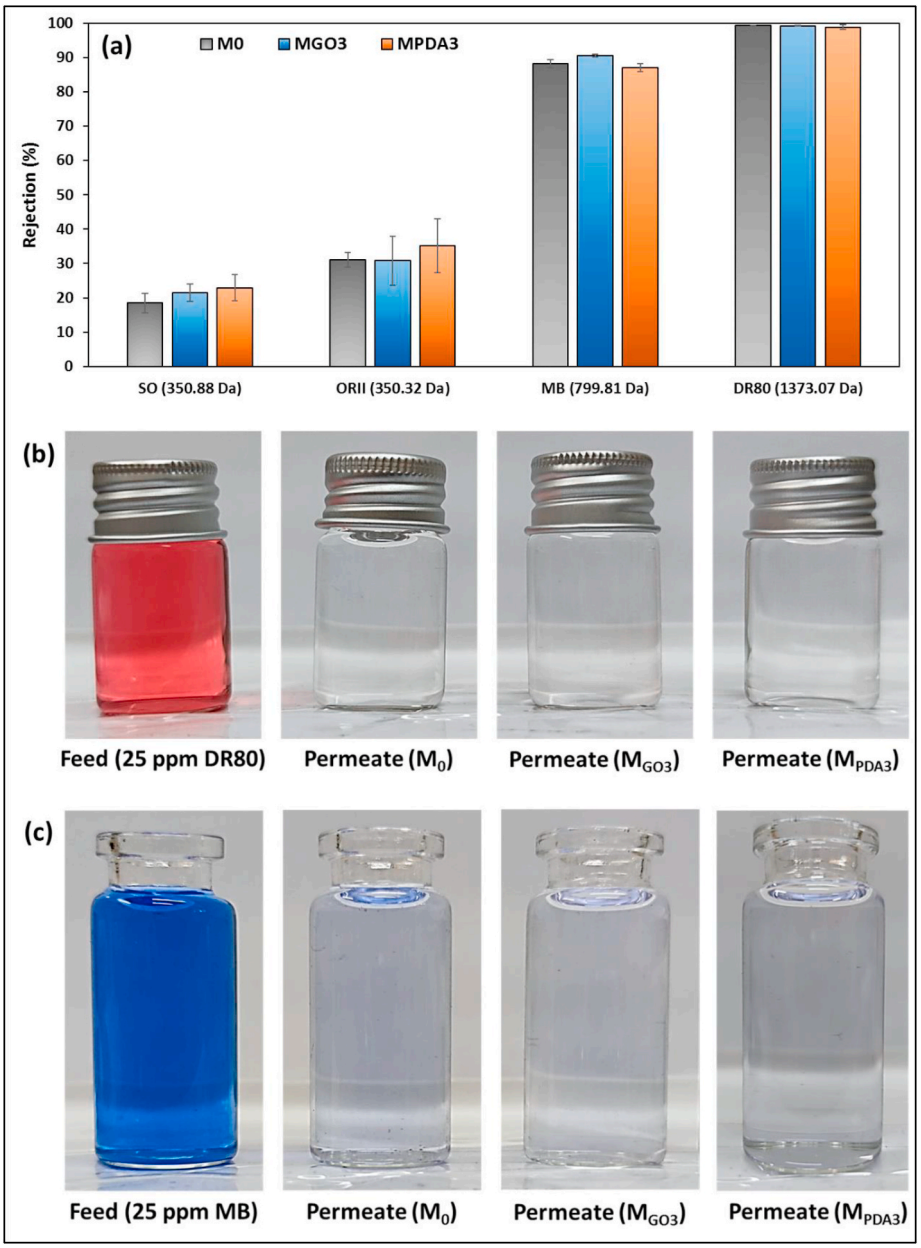

Fig. 10. (a) Dyes rejection performance of M_0, M_{GO3}, and M_{PDA3} (25 ppm dye concentration, 1 bar), photographs of the feed and permeate sample from the filtration experiments of (b) DR80 and (c) MB dyes.

four other aqueous solutions containing different dyes with small molecules were tested and presented in Fig. 10a. The SO (350.88 Da) and ORII (350.32 Da) dyes were tested to find the rejection properties of the two dyes as they have almost similar molecular weight. The rejection of SO dye ranged between 18.5 and 22.9% while the ORII dye rejection ranged between 31.1 and 35.2%. This could be to the higher affinity of the prepared membranes to reject the negatively charged molecules (e.g. ORII) than the positively charged molecules (e.g. SO). PSF membranes were reported in several studies to exhibit negative surface charge at pH > 6 [62]. The rejection of the MB (799.81 Da) was found to be 88.2 ± 1.2, 90.6 ± 0.4, and 87 ± 1.2% with M_0, M_{GO3}, and M_{PDA3}, respectively; while all these membranes exhibited excellent rejection (>98.5%) of DR80 (1373.07 Da). Fig. 10b and c shows photographs of the feed and permeate samples during the filtration of DR80 and MB dyes, respectively. It can be clearly seen from the dyes rejection results that the pristine PSF and the composite membranes exhibit almost similar rejection performance regardless of the differences in their water fluxes. Also, the rejection values of DR80 and MB are considered high for ultrafiltration membranes. This performance was reported with some GO-based UF membranes against low molecular weight dyes such as PES/GO (~ 90% rejection of Sunset Yellow dye, 452.4 Da) [10], PVDF/rGO-SiO_2 and CA/rGO-PDA-g-C_3N_4 (99.8% rejection of Methylene Blue, 319.85 Da) [27,31]. These findings suggest that the separation is not only dependent on the physical sieving and might be affected by the surface charge and additional interactions (e.g. adsorption mechanisms), indicating that the prepared membranes can be utilized in the treatment of different types of wastewater.

3.4. Antifouling properties

The fouling resistance is one of the key properties of a good-performance membrane. The filtration process typically leads to the blockage of membrane pores, formation of cake layers on the membrane surface and concentration polarization [63]. In the current study, it was

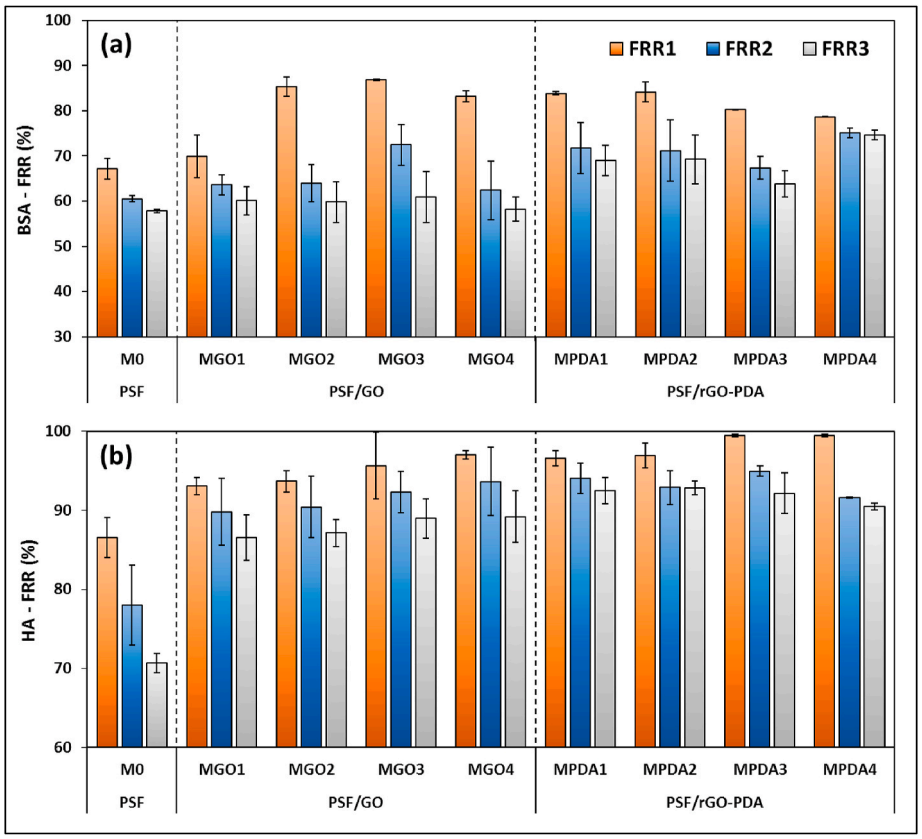

Fig. 11. The flux recovery ratio (FRR%) of the tested membranes against (a) BSA and (b) HA.

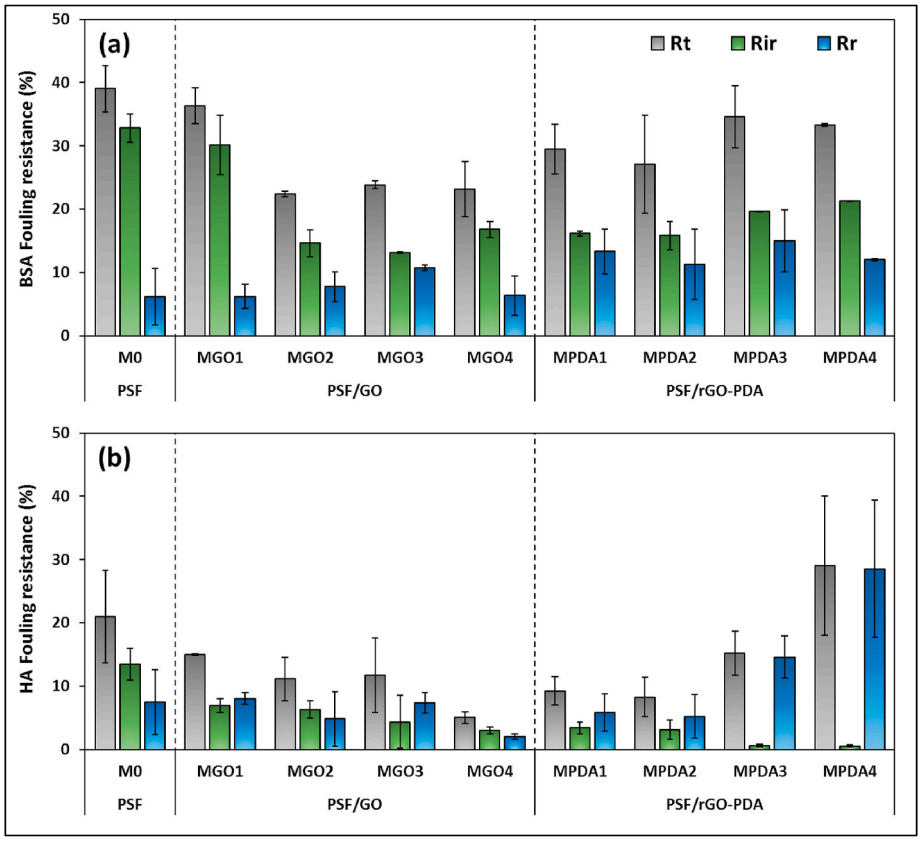

Fig. 12. The fouling resistance parameters (cycle 1) of the tested membranes against (a) BSA and (b) HA.

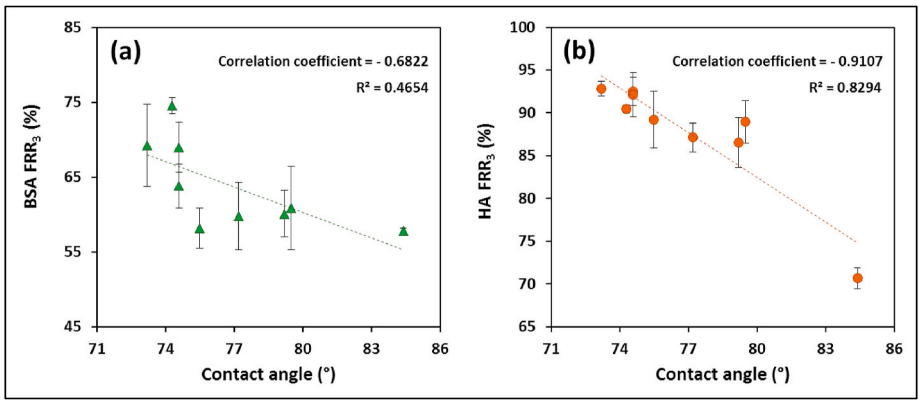

Fig. 13. The correlations of the (a) BSA FRR_3 and (b) HA FRR_3 with the contact angle.

observed that all membranes exhibited a flux decline after switching the feed from pure water to BSA or HA solutions. This can be attributed to the formation of foulant layers as a result of the deposition of BSA or HA molecules onto the membranes surface. After 30 min of membrane washing with DIW, the pure water flux was partially recovered for all membranes and the flux recovery ratio of the first fouling cycle (FRR_1) was then calculated. The second and third fouling cycles were performed under the same conditions (1 h filtration followed by 30 min washing) and the corresponding recovery values were calculated (FRR_2 and FRR_3). The antifouling performance of the tested membranes represented by their FRR against BSA and HA are depicted in Fig. 11a and b, respectively. Obviously, all PSF/GO and PSF/rGO-PDA composite membranes exhibited higher FRR compared to the pristine PSF. FRR_1, FRR_2, and FRR_3 of the pristine PSF against BSA were found to be 67.2 ± 2.2%, 60.5 ± 0.7, and 57.8 ± 0.4%, respectively. M_{GO3} (PSF/GO-0.1) exhibited the highest recovery ratio in the first cycle (86.9 ± 0.1%) and then decreased to 72.5 ± 4.5% and 60.9 ± 5.6% in the second and third cycles, respectively. The highest BSA-FRR among the PSF/rGO-PDA composite membranes were obtained with M_{PDA2} (PSF/rGO-PDA-0.05) with FRR_1, FRR_2, and FRR_3 of 84.2 ± 2.2%, 71.2 ± 6.8%, and 69.2 ± 3.3%, respectively. Interestingly, after 3 cycles of protein fouling, the flux recovery (FRR_3) of PSF/rGO-PDA composites were found to be higher than those of PSF/GO composites indicating higher antifouling stability of rGO-PDA based composites in long runs. When using HA as the model foulant, the flux recovery ratios of the pristine PSF were found to be 86.5 ± 2.5%, 78.0 ± 5.1% and 70.7 ± 1.2% for FRR_1, FRR_2, and FRR_3, respectively. The highest HA antifouling properties were obtained with M_{PDA3} (PSF/rGO-PDA-0.1) that achieved 99.4 ± 0.2%, 94.9 ± 0.7%, and 92.1 ± 2.6% for FRR_1, FRR_2, and FRR_3, respectively. The highest FRRs among the PSF/GO composites was obtained with M_{GO4} (PSF/GO-0.15) with 97.0 ± 0.5%, 93.6 ± 4.3%, and 89.2 ± 3.3% for FRR_1, FRR_2, and FRR_3, respectively.

For further analysis of the fouling resistance of the tested membranes, R_t, R_r and R_{ir} of cycle 1 were estimated and presented in Fig. 12a and b for BSA and HA, respectively. As depicted by Fig. 12a, all composite membranes exhibited lower total fouling ratio (R_t) and irreversible fouling ratio (R_{ir}) with higher reversible ratio (R_r) compared to those of the pristine PSF against BSA. The reversible fouling (R_r) of the pristine PSF was 6.2% which was elevated to 10.8% and 15% with 0.1 wt% addition of GO and rGO-PDA, respectively. With HA fouling, the reversible fouling ratio was not enhanced with GO addition, while it was elevated up to 14.6% and 28.5% with the addition of 0.1 and 0.15 wt% rGO-PDA, respectively, compared to 7.5% of the pristine PSF. These results indicate higher fouling resistance against protein and organic fouling of the PSF/rGO-PDA composite membranes compared to the pristine PSF and PSF/GO composite membranes.

It is well established that both surface hydrophilicity and roughness affect the membranes antifouling properties [16]. As elaborated in the morphological study above, both PSF/GO and PSF/rGO-PDA composites showed higher surface roughness and hydrophilicity than the pristine PSF. Therefore, in the first stage of foulant filtration, foulant molecules accumulate in the valleys and the pores because of the high surface roughness leading to clear reduction in the flux. During the washing step with water, GO and rGO-PDA particles attached to the pores and on the surface enhance the removal of foulants by water due to their hydrophilicity [16,61,64]. Therefore, the FRRs of all composite membranes were higher than this of the pristine PSF. Similar observations were reported by Yang et al. where the FRR increased disregards the increase in surface roughness [65]. To further investigate the effect of hydrophilicity on the membranes fouling resistance, the correlation coefficient between FRR_3 and CA was calculated and depicted in Fig. 13. Clearly, the resistance against both foulants are affected by the membrane's hydrophilicity. The HA fouling resistance is highly dependent on the hydrophilicity as shown in Fig. 13b, while the BSA FRR_3 have lower correlation. This can be explained by the penetration and accumulation of BSA molecules into the pores, which impedes their removal during the membrane washing. In contrast, HA molecules have lower possibility to penetrate into the pores due to their higher molecular sizes and hence can be easily washed out from the surface [66]. Consequently, it can be concluded from these results that the antifouling properties, of these membranes, were enhanced by the hydrophilic nature of GO and rGO-PDA particles. Fig. 14 shows photographs of the washed pristine PSF, M_{GO4}, and M_{PDA4} after the third fouling cycle with HA. The photographs of BSA-fouled membranes were not shown as BSA is almost colorless on membrane surface.

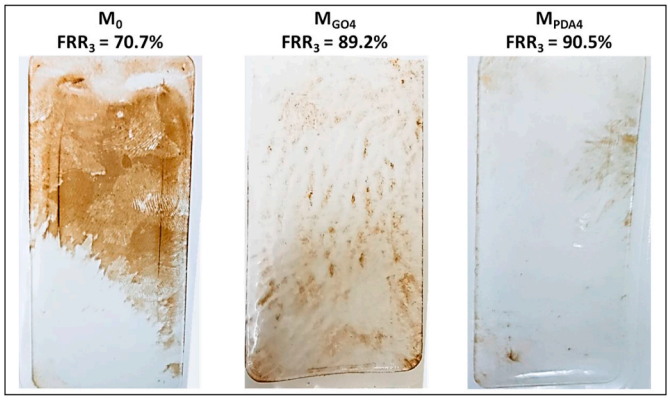

Fig. 14. Photographs of M_0, M_{GO4}, and M_{PDA4} after the third cycle of HA fouling.

Table 3 compares the performance of M_{GO3} (PSF/GO-0.1) and M_{PDA3} (PSF/rGO-PDA-0.1) with other UF composite membranes in literature that are synthesized via the phase inversion approach. The comparison

Table 3
Performance comparison of the MMMs prepared in this work with other GO-based UF MMMs prepared by phase inversion in literature.

Membrane	Foulant composition (ppm)	Conditions	PWP (LMH/bar)	Rejection %	FRR_1%	Ref.
PES/CSGO	1000 ppm BSA	Dead-end, 2 bar, 1 h	41.3	99.8	92.1	2020 [17]
PSF/GO	1000 ppm BSA	Cross-flow, 1 bar, 100 min	352.2	88.6	71.9	2020 [12]
PVDF/PFSA-g-GO	500 ppm BSA and HA	Dead-end, 1 bar, 30 min	587.4	$R_{BSA} = 93.9$ $R_{HA} = 79.6$	90.8	2020 [68]
PSF/GFG	200 ppm BSA	Cross-flow, 1 bar, 1 h	217	95.2	82.4	2019 [15]
PES/SPSF/GO	1000 ppm BSA	Cross-flow, 1 bar, 1 h	816.9	99.5	94.2	2019 [9]
PSF/CGO	1000 ppm BSA, 10 ppm Methyl Orange (MO) dye	Dead-end, 1 bar, 2 h	48.8 ± 3.7	$R_{BSA} = 100$ $R_{MO} = 52.7$	76.3 ± 17	2019 [13]
PES/GO	50 ppm HA	Dead-end, 1 bar, 2 h	340	94.5	95	2019 [36]
PVDF/TiO_2-GO	1000 ppm BSA	Cross-flow, 1 bar	199.97	91.38	89.22	2019 [67]
PES/GO	1000 ppm BSA	Dead-end, 1 bar, 30 min	245	97	75	2018 [10]
PSF/Fe_3O_4-GO	20 ppm HA	Dead-end, 1 bar	156.99	84	–	2017 [69]
PVC/GO	1000 ppm BSA	Dead-end, 1 bar, 20 min	430	91.2	70.4	2016 [11]
PES/GO-Ag	500 ppm BSA	Dead-end, 3 bar, 90 min	143.3	98	67.2	2015 [70]
PES/Co_3O_4-GO	1000 ppm BSA	Dead-end, 1 bar, 2 h	347.9	95	81.1	2015 [52]
PVDF/GO-APTS	1000 ppm BSA	Dead-end, 1 bar, 1 h	401.39	57	>95	2014 [16]
BPPO/PEI-GO	500 ppm BSA	Cross-flow, 2 bar, 1 h	532.5	91	63	2014 [65]
PVDF/GO	1000 ppm BSA	Dead-end, 1 bar	~90	~85	90	2014 [8]
PSF/Isocyanate-GO	1000 ppm BSA	Cross-flow, 1 bar, 2 h	135	95	40.27	2013 [18]
PSF/rGO-PDA-0.1	500 ppm BSA 25 ppm HA 25 ppm SO, ORII, MB and DR80 dyes	Cross-flow, 1 bar, 1 h	326.5 ± 10.3	$R_{BSA} = R_{HA} = 100$ $R_{SO} = 22.9 \pm 3.8$ $R_{ORII} = 35.2 \pm 7.8$ $R_{MB} = 87 \pm 1.2$ $R_{DR80} = 98.8 \pm 0.7$	$FRR_{BSA} = 80.4$ $FRR_{HA} = 99.4 \pm 0.2$	Present study
PSF/GO-0.1			164.5 ± 2.7	$R_{BSA} = R_{HA} = 100$ $R_{SO} = 21.5 \pm 2.5$ $R_{ORII} = 30.8 \pm 7.1$ $R_{MB} = 90.6 \pm 0.4$ $R_{DR80} = 99.2 \pm 0.1$	$FRR_{BSA} = 86.9 \pm 0.1$ $FRR_{HA} = 95.4 \pm 4.2$	

was performed in terms of PWP, rejection, and FRR_1. Obviously, M_{GO3} and M_{PDA3} perform as well as or better than most of these membranes. It can be clearly noticed from the table that composite membranes incorporating pristine GO particles [10–12,65] suffer from the low FRR (<75%) against BSA fouling. In contrast, composite membranes embedding functional GO structures like CSGO [17], TiO_2-GO [67], and GO-APTS [16] generally exhibit high fouling resistance (~ 90%) but suffer from the low rejection or flux. Commonly, composite membranes with high flux exhibit lower rejection and fouling resistance and vice versa. However, a recent study by Hu et al. [9] reported high performing membranes with respect to flux, rejection and FRR.

4. Conclusion

In this work, polydopamine functionalized GO (rGO-PDA) particles were used as nanofiller to produce novel ultrafiltration PSF MMMs. Starting from natural graphite, GO particles were prepared and then reduced and functionalized during the self-polymerization of dopamine (DA). The success of functionalization reaction was confirmed using different analytical techniques including FTIR, Raman spectra, XPS, and SEM. Via the phase inversion technique, two types of MMMs were synthesized incorporating different loadings of the pristine GO and the rGO-PDA particles for comparison purposes. Obvious differences in the pore structure were observed by the cross-section SEM images. The pristine GO particles were found to agglomerate in the pores and some regions of the polymer matrix resulting in flux decline with the increase of GO loading. In contrast, better distribution of rGO-PDA particles in the PSF matrix was confirmed by the SEM images owing to the high dispersity of rGO-PDA in NMP. The enhancement of pore structure, hydrophilicity and surface roughness resulted in a high pure water flux that is approximately 1.8 and 2 times higher than the pristine PSF and PSF/GO-0.1, respectively. The rejection performance of the prepared membranes was explored by the filtration of BSA, HA, and different dyes having different molecular weights. The results showed almost similar rejection performance of the pristine PSF and the composite membranes. Furthermore, after 3 protein fouling cycles, the highest FRR was obtained with PSF/rGO-PDA-0.1 (74.6%) that was 29% and 22% higher than this of the pristine PSF and PSF/GO-0.1. FRR_3 of PSF/rGO-PDA-0.1 was also higher than the pristine PSF and PSF/GO-0.1 by 30% and 3%, respectively. Taken together, results reported in this work showed that the incorporation of rGO-PDA particles could greatly enhance the flux and antifouling properties of PSF ultrafiltration membranes without affecting the rejection performance. The results reported herein are expected to be of a great benefit in protein-rich and NOMs-rich wastewater treatment and provide insights on developing other rGO-PDA based membranes with different materials and for different purposes.

Declaration of competing interest

The authors declare that they have no known competing financial interests or personal relationships that could have appeared to influence the work reported in this paper.

Acknowledgment

This work was made possible by an Award [GSRA4-1-0504-17043] from Qatar National Research Fund (QNRF, a member of Qatar Foundation). The contents herein are solely the responsibility of the authors. Authors would like to thank also the Central Lab Unit (CLU) at Qatar University (QU) for carrying out the FTIR-UATR, Raman spectroscopy, and SEM; Gas Processing Center (GPC, QU) for the XPS analysis and viscosity measurements; and Center of Advanced Materials (CAM, QU) for their support in AFM analysis. Open access funding is provided by Qatar National Library.

Appendix A. Supplementary data

Supplementary data to this article can be found online at https://doi.org/10.1016/j.memsci.2020.118900.

References

[1] Z. Yang, X.-H. Ma, C.Y. Tang, Recent development of novel membranes for desalination, Desalination 434 (2018) 37–59.
[2] M. Yao, L.D. Tijing, G. Naidu, S.-H. Kim, H. Matsuyama, A.G. Fane, H.K. Shon, A review of membrane wettability for the treatment of saline water deploying membrane distillation, Desalination 479 (2020) 114312.
[3] M.A. Hafiz, A.H. Hawari, A. Altaee, A hybrid forward osmosis/reverse osmosis process for the supply of fertilizing solution from treated wastewater, J. Water Process Eng. 32 (2019) 100975.
[4] N. Hilal, G. Busca, N. Hankins, A.W. Mohammad, The use of ultrafiltration and nanofiltration membranes in the treatment of metal-working fluids, Desalination 167 (2004) 227–238.
[5] K.P. Lee, T.C. Arnot, D. Mattia, A review of reverse osmosis membrane materials for desalination—development to date and future potential, J. Membr. Sci. 370 (2011) 1–22.
[6] N. Song, X. Gao, Z. Ma, X. Wang, Y. Wei, C. Gao, A review of graphene-based separation membrane: materials, characteristics, preparation and applications, Desalination 437 (2018) 59–72.
[7] M.M. Pendergast, E.M.V. Hoek, A review of water treatment membrane nanotechnologies, Energy Environ. Sci. 4 (2011) 1946–1971.
[8] X. Chang, Z. Wang, S. Quan, Y. Xu, Z. Jiang, L. Shao, Exploring the synergetic effects of graphene oxide (GO) and polyvinylpyrrodione (PVP) on poly (vinylidenefluoride) (PVDF) ultrafiltration membrane performance, Appl. Surf. Sci. 316 (2014) 537–548.
[9] M. Hu, Z. Cui, J. Li, L. Zhang, Y. Mo, D.S. Dlamini, H. Wang, B. He, J. Li, H. Matsuyama, Ultra-low graphene oxide loading for water permeability, antifouling and antibacterial improvement of polyethersulfone/sulfonated polysulfone ultrafiltration membranes, J. Colloid Interface Sci. 552 (2019) 319–331.
[10] A. Abdel-Karim, S. Leaper, M. Alberto, A. Vijayaraghavan, X. Fan, S.M. Holmes, E. R. Souaya, M.I. Badawy, P. Gorgojo, High flux and fouling resistant flat sheet polyethersulfone membranes incorporated with graphene oxide for ultrafiltration applications, Chem. Eng. J. 334 (2018) 789–799.
[11] Y. Zhao, J. Lu, X. Liu, Y. Wang, J. Lin, N. Peng, J. Li, F. Zhao, Performance enhancement of polyvinyl chloride ultrafiltration membrane modified with graphene oxide, J. Colloid Interface Sci. 480 (2016) 1–8.
[12] R.S. Zambare, K.B. Dhopte, P.R. Nemade, C.Y. Tang, Effect of oxidation degree of GO nanosheets on microstructure and performance of polysulfone-GO mixed matrix membranes, Separ. Purif. Technol. 244 (2020) 116865.
[13] Y. Jiang, Q. Zeng, P. Biswas, J.D. Fortner, Graphene oxides as nanofillers in polysulfone ultrafiltration membranes: shape matters, J. Membr. Sci. 581 (2019) 453–461.
[14] S. Chatterjee, F. Nafezarefi, N.H. Tai, L. Schlagenhauf, F.A. Nüesch, B.T.T. Chu, Size and synergy effects of nanofiller hybrids including graphene nanoplatelets and carbon nanotubes in mechanical properties of epoxy composites, Carbon 50 (2012) 5380–5386.
[15] G. Zhang, M. Zhou, Z. Xu, C. Jiang, C. Shen, Q. Meng, Guanidyl-functionalized graphene/polysulfone mixed matrix ultrafiltration membrane with superior permselective, antifouling and antibacterial properties for water treatment, J. Colloid Interface Sci. 540 (2019) 295–305.
[16] Z. Xu, J. Zhang, M. Shan, Y. Li, B. Li, J. Niu, B. Zhou, X. Qian, Organosilane-functionalized graphene oxide for enhanced antifouling and mechanical properties of polyvinylidene fluoride ultrafiltration membranes, J. Membr. Sci. 458 (2014) 1–13.
[17] S. Kong, M.-y. Lim, H. Shin, J.-H. Baik, J.-C. Lee, High-flux and antifouling polyethersulfone nanocomposite membranes incorporated with zwitterion-functionalized graphene oxide for ultrafiltration applications, J. Ind. Eng. Chem. 84 (2020) 131–140.
[18] H. Zhao, L. Wu, Z. Zhou, L. Zhang, H. Chen, Improving the antifouling property of polysulfone ultrafiltration membrane by incorporation of isocyanate-treated graphene oxide, Phys. Chem. Chem. Phys. 15 (2013) 9084–9092.
[19] H. Lee, S.M. Dellatore, W.M. Miller, P.B. Messersmith, Mussel-inspired surface chemistry for multifunctional coatings, Science 318 (2007) 426–430.
[20] S. Palanisamy, B. Thirumalraj, S.-M. Chen, Y.-T. Wang, V. Velusamy, S.K. Ramaraj, A facile electrochemical preparation of reduced graphene Oxide@Polydopamine composite: a novel electrochemical sensing platform for amperometric detection of chlorpromazine, Sci. Rep. 6 (2016) 33599.
[21] T. Wang, H. Qiblawey, E. Sivaniah, A. Mohammadian, Novel methodology for facile fabrication of nanofiltration membranes based on nucleophilic nature of polydopamine, J. Membr. Sci. 511 (2016) 65–75.
[22] T. Wang, H. Qiblawey, S. Judd, A. Benamor, M.S. Nasser, A. Mohammadian, Fabrication of high flux nanofiltration membrane via hydrogen bonding based co-deposition of polydopamine with poly(vinyl alcohol), J. Membr. Sci. 552 (2018) 222–233.
[23] L. Zhang, Y. Lin, S. Wang, L. Cheng, H. Matsuyama, Engineering of ultrafine polydopamine nanoparticles in-situ assembling on polyketone substrate for highly-efficient oil-water emulsions separation, J. Membr. Sci. 613 (2020) 118501.
[24] Z. Zhou, B. Zheng, Y. Gu, C. Shen, J. Wen, Z. Meng, S. Chen, J. Ou, A. Qin, New approach for improving anticorrosion and biocompatibility of magnesium alloys via polydopamine intermediate layer-induced hydroxyapatite coating, Surf. Interf. 19 (2020) 100501.
[25] S. Yang, M. Liu, F. Deng, L. Mao, S. Yu, H. Huang, J. Chen, L. Liu, X. Zhang, Y. Wei, A novel fluorescent DNA sensor system based on polydopamine modified MgAl-layered double hydroxides, Coll. Interf. Sci. Commun. 37 (2020) 100294.
[26] D. Cheng, X. Bai, J. Pan, J. Ran, J. Wu, S. Bi, G. Cai, X. Wang, Immobilizing reduced graphene oxide on polydopamine-templated PET fabrics for UV protection, electrical conduction and application as wearable sensors, Mater. Chem. Phys. 241 (2020) 122371.
[27] F. Li, Z. Yu, H. Shi, Q. Yang, Q. Chen, Y. Pan, G. Zeng, L. Yan, A Mussel-inspired method to fabricate reduced graphene oxide/g-C3N4 composites membranes for catalytic decomposition and oil-in-water emulsion separation, Chem. Eng. J. 322 (2017) 33–45.
[28] L.Q. Xu, W.J. Yang, K.-G. Neoh, E.-T. Kang, G.D. Fu, Dopamine-Induced reduction and functionalization of graphene oxide nanosheets, Macromolecules 43 (2010) 8336–8339.
[29] Y. Liu, D. Gan, M. Chen, L. Ma, B. Yang, L. Li, M. Zhu, W. Tu, Bioinspired dopamine modulating graphene oxide nanocomposite membrane interposed by super-hydrophilic UiO-66 with enhanced water permeability, Separ. Purif. Technol. 253 (2020) 117552.
[30] Z. Liu, W. Wu, Y. Liu, C. Qin, M. Meng, Y. Jiang, J. Qiu, J. Peng, A mussel inspired highly stable graphene oxide membrane for efficient oil-in-water emulsions separation, Separ. Purif. Technol. 199 (2018) 37–46.
[31] Y. Peng, Z. Yu, F. Li, Q. Chen, D. Yin, X. Min, A novel reduced graphene oxide-based composite membrane prepared via a facile deposition method for multifunctional applications: oil/water separation and cationic dyes removal, Separ. Purif. Technol. 200 (2018) 130–140.
[32] A. Alkhouzaam, H. Qiblawey, M. Khraisheh, M. Atieh, M. Al-Ghouti, Synthesis of graphene oxides particle of high oxidation degree using a modified Hummers method, Ceram. Int. 46 (2020) 23997–24007.
[33] A. Alkhouzaam, M. Khraisheh, M. Atilhan, S.A. Al-Muhtaseb, L. Qi, D. Rooney, High-pressure CO 2/N 2 and CO 2/CH 4 separation using dense polysulfone-supported ionic liquid membranes, J. Nat. Gas Sci. Eng. 36 (2016) 472–485.
[34] S. Ayyaru, Y.-H. Ahn, Application of sulfonic acid group functionalized graphene oxide to improve hydrophilicity, permeability, and antifouling of PVDF nanocomposite ultrafiltration membranes, J. Membr. Sci. 525 (2017) 210–219.
[35] J. Tian, M. Pan, Y. Ma, J.W. Chew, Effect of membrane fouling on chiral separation, J. Membr. Sci. 593 (2020) 117352.
[36] M.S. Algamdi, I.H. Alsohaimi, J. Lawler, H.M. Ali, A.M. Aldawsari, H.M.A. Hassan, Fabrication of graphene oxide incorporated polyethersulfone hybrid ultrafiltration membranes for humic acid removal, Separ. Purif. Technol. 223 (2019) 17–23.
[37] R. Muzyka, M. Kwoka, Ł. Smędowski, N. Díez, G. Gryglewicz, Oxidation of graphite by different modified Hummers methods, N. Carbon Mater. 32 (2017) 15–20.
[38] A. Thakur, S. Ranote, D. Kumar, K.K. Bhardwaj, R. Gupta, G.S. Chauhan, Synthesis of a PEGylated dopamine ester with enhanced antibacterial and antifungal activity, ACS Omega 3 (2018) 7925–7933.
[39] M. Faraji, H. Gharibi, M. Javaheri, High Pt loading on polydopamine functionalized graphene as a high performance cathode electrocatalyst for proton exchange membrane fuel cells, J. Nanostruct. 6 (2016) 156–166.
[40] S.E. Lowe, G. Shi, Y. Zhang, J. Qin, L. Jiang, S. Jiang, M. Al-Mamun, P. Liu, Y. L. Zhong, H. Zhao, The role of electrolyte acid concentration in the electrochemical exfoliation of graphite: mechanism and synthesis of electrochemical graphene oxide, Nano Mater. Sci. 1 (3) (2019) 215–223.
[41] M. Khraisheh, K.M. Zadeh, A.I. Alkhouzaam, D. Turki, M.K. Hassan, F.A. Momani, S.M.J. Zaidi, Characterization of polysulfone/diisopropylamine 1-alkyl-3-methylimidazolium ionic liquid membranes: high pressure gas separation applications, Greenhouse Gases: Sci. Technol. 10 (2020) 795–808.
[42] Y. Kang, M. Obaid, J. Jang, M.-H. Ham, I.S. Kim, Novel sulfonated graphene oxide incorporated polysulfone nanocomposite membranes for enhanced-performance in ultrafiltration process, Chemosphere 207 (2018) 581–589.
[43] S. Zinadini, A.A. Zinatizadeh, M. Rahimi, V. Vatanpour, H. Zangeneh, Preparation of a novel antifouling mixed matrix PES membrane by embedding graphene oxide nanoplates, J. Membr. Sci. 453 (2014) 292–301.
[44] J. Zhang, Z. Xu, M. Shan, B. Zhou, Y. Li, B. Li, J. Niu, X. Qian, Synergetic effects of oxidized carbon nanotubes and graphene oxide on fouling control and anti-fouling mechanism of polyvinylidene fluoride ultrafiltration membranes, J. Membr. Sci. 448 (2013) 81–92.
[45] S. Bandehali, A. Moghadassi, F. Parvizian, Y. Zhang, S.M. Hosseini, J. Shen, New mixed matrix PEI nanofiltration membrane decorated by glycidyl-POSS functionalized graphene oxide nanoplates with enhanced separation and antifouling behaviour: heavy metal ions removal, Separ. Purif. Technol. 242 (2020) 116745.
[46] K.-J. Lu, J. Zuo, T.-S. Chung, Novel PVDF membranes comprising n-butylamine functionalized graphene oxide for direct contact membrane distillation, J. Membr. Sci. 539 (2017) 34–42.
[47] M.R. Jamalludin, Z. Harun, S.K. Hubadillah, H. Basri, A.F. Ismail, M.H.D. Othman, M.F. Shohur, M.Z. Yunos, Antifouling polysulfone membranes blended with green SiO2 from rice husk ash (RHA) for humic acid separation, Chem. Eng. Res. Des. 114 (2016) 268–279.
[48] Y. Mu, H. Feng, S. Zhang, C. Zhang, N. Lu, J. Luan, G. Wang, Development of highly permeable and antifouling ultrafiltration membranes based on the synergistic effect of carboxylated polysulfone and bio-inspired co-deposition modified hydroxyapatite nanotubes, J. Colloid Interface Sci. 572 (2020) 48–61.

[49] M.B.M.Y. Ang, C.R.M. Macni, A.R. Caparanga, S.-H. Huang, H.-A. Tsai, K.-R. Lee, J.-Y. Lai, Mitigating the fouling of mixed-matrix cellulose acetate membranes for oil–water separation through modification with polydopamine particles, Chem. Eng. Res. Des. 159 (2020) 195–204.
[50] A. Rahimpour, M. Jahanshahi, S. Khalili, A. Mollahosseini, A. Zirepour, B. Rajaeian, Novel functionalized carbon nanotubes for improving the surface properties and performance of polyethersulfone (PES) membrane, Desalination 286 (2012) 99–107.
[51] J. Zhang, Z. Xu, W. Mai, C. Min, B. Zhou, M. Shan, Y. Li, C. Yang, Z. Wang, X. Qian, Improved hydrophilicity, permeability, antifouling and mechanical performance of PVDF composite ultrafiltration membranes tailored by oxidized low-dimensional carbon nanomaterials, J. Mater. Chem. 1 (2013) 3101–3111.
[52] G. Ouyang, A. Hussain, J. Li, D. Li, Remarkable permeability enhancement of polyethersulfone (PES) ultrafiltration membrane by blending cobalt oxide/graphene oxide nanocomposites, RSC Adv. 5 (2015) 70448–70460.
[53] M. Akbari, M. Shariaty-Niassar, T. Matsuura, A.F. Ismail, Janus graphene oxide nanosheet: a promising additive for enhancement of polymeric membranes performance prepared via phase inversion, J. Colloid Interface Sci. 527 (2018) 10–24.
[54] S. Xia, M. Ni, Preparation of poly(vinylidene fluoride) membranes with graphene oxide addition for natural organic matter removal, J. Membr. Sci. 473 (2015) 54–62.
[55] L. Yu, Y. Zhang, B. Zhang, J. Liu, H. Zhang, C. Song, Preparation and characterization of HPEI-GO/PES ultrafiltration membrane with antifouling and antibacterial properties, J. Membr. Sci. 447 (2013) 452–462.
[56] H. Sun, B. Tang, P. Wu, Development of hybrid ultrafiltration membranes with improved water separation properties using modified superhydrophilic metal–organic framework nanoparticles, ACS Appl. Mater. Interfaces 9 (2017) 21473–21484.
[57] A. Alammar, S.-H. Park, C.J. Williams, B. Derby, G. Szekely, Oil-in-water separation with graphene-based nanocomposite membranes for produced water treatment, J. Membr. Sci. 603 (2020) 118007.
[58] E. Fontananova, V. Grosso, S.A. Aljlil, M.A. Bahattab, D. Vuono, F.P. Nicoletta, E. Curcio, E. Drioli, G. Di Profio, Effect of functional groups on the properties of multiwalled carbon nanotubes/polyvinylidenefluoride composite membranes, J. Membr. Sci. 541 (2017) 198–204.
[59] M.-l. Luo, W. Tang, J.-q. Zhao, C.-s. Pu, Hydrophilic modification of poly(ether sulfone) used TiO2 nanoparticles by a sol–gel process, J. Mater. Process. Technol. 172 (2006) 431–436.
[60] A. Razmjou, J. Mansouri, V. Chen, The effects of mechanical and chemical modification of TiO2 nanoparticles on the surface chemistry, structure and fouling performance of PES ultrafiltration membranes, J. Membr. Sci. 378 (2011) 73–84.
[61] J. Lee, H.-R. Chae, Y.J. Won, K. Lee, C.-H. Lee, H.H. Lee, I.-C. Kim, J.-m. Lee, Graphene oxide nanoplatelets composite membrane with hydrophilic and antifouling properties for wastewater treatment, J. Membr. Sci. 448 (2013) 223–230.
[62] A. Khan, T.A. Sherazi, Y. Khan, S. Li, S.A.R. Naqvi, Z. Cui, Fabrication and characterization of polysulfone/modified nanocarbon black composite antifouling ultrafiltration membranes, J. Membr. Sci. 554 (2018) 71–82.
[63] W. Gao, H. Liang, J. Ma, M. Han, Z.-l. Chen, Z.-s. Han, G.-b. Li, Membrane fouling control in ultrafiltration technology for drinking water production: a review, Desalination 272 (2011) 1–8.
[64] T. Hwang, J.-S. Oh, W. Yim, J.-D. Nam, C. Bae, H.-i. Kim, K.J. Kim, Ultrafiltration using graphene oxide surface-embedded polysulfone membranes, Separ. Purif. Technol. 166 (2016) 41–47.
[65] L. Yang, B. Tang, P. Wu, UF membrane with highly improved flux by hydrophilic network between graphene oxide and brominated poly(2,6-dimethyl-1,4-phenylene oxide), J. Mater. Chem. 2 (2014) 18562–18573.
[66] B. Saini, M.K. Sinha, S.K. Dash, Mitigation of HA, BSA and oil/water emulsion fouling of PVDF Ultrafiltration Membranes by SiO2-g-PEGMA nanoparticles, J. Water Process Eng. 30 (2019) 100603.
[67] L.-g. Wu, X.-y. Zhang, T. Wang, C.-h. Du, C.-h. Yang, Enhanced performance of polyvinylidene fluoride ultrafiltration membranes by incorporating TiO2/graphene oxide, Chem. Eng. Res. Des. 141 (2019) 492–501.
[68] X. Liu, H. Yuan, C. Wang, S. Zhang, L. Zhang, X. Liu, F. Liu, X. Zhu, S. Rohani, C. Ching, J. Lu, A novel PVDF/PFSA-g-GO ultrafiltration membrane with enhanced permeation and antifouling performances, Separ. Purif. Technol. 233 (2020) 116038.
[69] P.V. Chai, E. Mahmoudi, Y.H. Teow, A.W. Mohammad, Preparation of novel polysulfone-Fe3O4/GO mixed-matrix membrane for humic acid rejection, J. Water Process Eng. 15 (2017) 83–88.
[70] V. Vatanpour, A. Shockravi, H. Zarrabi, Z. Nikjavan, A. Javadi, Fabrication and characterization of anti-fouling and anti-bacterial Ag-loaded graphene oxide/polyethersulfone mixed matrix membrane, J. Ind. Eng. Chem. 30 (2015) 342–352.